Nanoscale

Accepted Manuscript

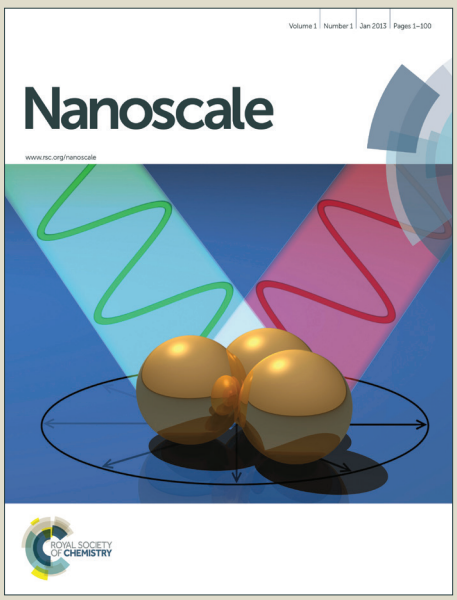

ROYAL SOCIETY OF CHEMISTRY

www.rsc.org/nanoscale

Journal Name

RSCPublishing

ARTICLE

Mapping Fullerene Crystallization in a Photovoltaic Blend: An Electron Tomography Study

Cite this: DOI: 10.1039/xoxxoooooox

Olof Bäcke,[a] Camilla Lindqvist,[b] Amaia Diaz de Zerio Mendaza,[b] Stefan Gustafsson,[a] Ergang Wang,[b] Mats R. Andersson,[b] Christian Müller,[b] Eva Olsson[a]*

Received ooth January xxxx,
Accepted ooth January xxxx

DOI: 10.1039/xoxxoooooox

www.rsc.org/

The formation of fullerene crystals represents a major degradation pathway of polymer/fullerene bulk-heterojunction thin films that inexorably deteriorates their photovoltaic performance. Currently no tools exist that reveal the origin of fullerene crystal formation vertically through the film. Here, we show that electron tomography can be used to study nucleation and growth of fullerene crystals. A model bulk-heterojunction blend based on a thiophene-quinoxaline copolymer and a fullerene derivative is examined after controlled annealing above the glass transition temperature. We image a number of fullerene nanocrystals, ranging in size from 100 to 400 nanometers, and observe that their center is located close to the free-surface of spin-coated films. The results show that the nucleation of fullerene crystals predominately occurs in the upper part of the films. Moreover, electron tomography reveals that the nucleation is preceded by more pronounced phase separation of the blend components.

Background

In the search for inexpensive and efficient organic solar cells (OSC), devices using bulk heterojunction (BHJ) blends as an active layer have turned out to be the most promising candidates.[1] In a BHJ blend the electron donor and the acceptor, ideally, form a bicontinuous network on the nanoscale, in order to optimize both charge generation and extraction. Today single junction devices utilizing a BHJ architecture have been reported to exhibit power conversion efficiencies (PCE) of up to 9-10%.[2-8] While this is lower than the PCE of solar cells based on other strategies for harvesting solar power, the potentially low cost and ease of manufacturing at an industrial scale makes OSC an interesting alternative. One of several problems that is encountered when taking a OSC from the laboratory scale to large-scale manufacturing is the particular sensitivity of the nanostructure and ultimately the efficiency of the device with regard to elevated processing and operating temperatures.

A complication with BHJ blends is that they are not at thermal equilibrium and thus not thermally stable. When the glass transition temperature (T_g) of a blend is reached the nanostructure of the blend starts to coarsen.[9-12] This often results in a dramatic drop in PCE of a solar cell.[9, 13-15] This behaviour is problematic, because while, for many BHJ blends, heat treatment is not a necessary step to make a working device under controlled laboratory conditions, several heating cycles will be necessary if devices are to be produced at an industrial scale. In particular, heating permits rapid removal of the solvent used for printing the active layer, which increase throughput.[16] The glass transition temperature is affected by the choice of acceptor and donor and will thus differ between different BHJ blends. Several studies have been done on how the thermal stability of BHJ blends can be increased by choosing donor and acceptors with a high T_g.[17]

While different acceptors have been investigated the common choice for high performing devices are fullerenes, where the most well studied alternative is the fullerene derivative [6,6]-phenyl-C_{61}-butric acid methyl ester, (PCBM). Heat treated blends utilizing PCBM will not only suffer from coarsening of the nanostructure, increasing the spatial separation of electron donor and acceptor into different domains, but also from the fact that PCBM will start to form crystals.[13, 18, 19] These crystals can grow as big as several hundreds of micrometers, even millimeters, in the lateral direction and over a micrometer in height, which is much larger than the typical active layer film thickness of around 100 nm. Hence the formation of PCBM crystals is detrimental to the performance of OSC.[9, 12, 20] The T_g for PCBM is ~ 110-140 °C.[11, 21, 22] This means that blends including PCBM will usually have T_g that is well within the temperature range, i. e. 140 °C, that can be expected to be used in a heat treatment cycle and making it important to be able to control the growth of PCBM crystals.[11, 13, 16, 22, 23]

Nucleation and growth rate of PCBM crystals have been studied for a number of systems and it has been shown that various parameters influence the formation of fullerene crystals, such as the choice of donor, acceptor/donor ratio, solvent, and substrate.[13, 19, 24] This opens up the possibility of controlling crystal growth, potentially even harnessing it to increase efficiency, if the nucleation and crystal growth process can be understood. However, all studies carried out to date only investigate the lateral distribution of fullerene crystals. Methods that have been employed include various microscopy and X-ray spectroscopy techniques.[9, 10, 13, 24-27] In contrast, the vertical distribution of crystals has not been studied in detail with a direct imaging technique.

Thus, in this study transmission electron (TE) tomography is employed to investigate, for the first time, the vertical distribution of

fullerene crystals in a BHJ blend. Like other tomography techniques, TE tomography is based on using a collection of two-dimensional projections of an object to recreate the three-dimensional structure of the object. The images obtained using transmission electron microscopy (TEM) show two dimensional projections of the bulk of a sample, meaning that TE tomography can be used to reconstruct the three dimensional nanostructure of the bulk of BHJ blends. The high resolution of electron microscopy is a further advantage compared to other techniques that can be used to probe the three-dimensional structure of a sample. TE tomography has been used during the last few years to investigate the nanostructure of various different BHJ blends, successfully exploring the connection between the components of the blend, the nanostructure and the PCE.[28-35] While TEM is a useful method for investigating the nanostructure of BHJ blends, there are limitations. One limitation is that in most cases the blend consists of two very similar components that both scatter electrons weakly, which means that contrast between different phases in BHJ blends tend to be weak. Another limitation is that the fine nanostructure of BHJ blends and the fact that the structure is highly disordered can complicate identification of ordered domains in the blend; Most information about the three dimensional structure of the blend is likely to be lost when projected down to two dimensions.

In this study we demonstrate that TE tomography can be used to vertically resolve the nucleation and growth of PCBM crystals in spincoated BHJ films. As a model system for this study we chose to work with poly(2,3-bis-(3-octyloxyphenyl)quinoxaline-5,8-diyl-*alt*-thiophene-2,5-diyl) (TQ1) and PCBM. TQ1:PCBM blends can give rise to a PCE of up to 6-7%.[36-39] TQ1 is a non-crystalline polymer, which eases structural analysis. In a previous study we have shown that when a TQ1:PCBM blend is heat treated above its glass transition temperature, PCBM crystals start to form, which leads to a rapid decrease in performance.[13] Our TE tomography analysis permits us to establish that in the here investigated system PCBM nucleation occurs close to the free top surface of the spincoated films.

Experimental

Materials

$PC_{61}BM$ (purity > 99%) was purchased from Solenne BV. TQ1 was prepared according to previously published procedures.[36] (number-average molecular weight of $M_n \sim 71$ kg mol^{-1}; polydispersity index $PDI \sim 3.7$). PEDOT:PSS was purchased from Heraeus (Clevious P VP Al 4083) and used as received.

Thin film preparation

Films were spin-coated from *ortho*-dichlorobenzene (*o*DCB) solutions (total material content 20 g L-1). Glass substrates were coated with poly(3,4-thylenedioxythiophene):poly(styrenesulfonate) (PEDOT:PSS, Heraeus, Clevios P VP Al 4083) and annealed at 120 °C for 10 min prior to film deposition. The film thickness was ~ 95 nm as measured by AFM. Annealing was carried out at ambient atmosphere but absence of light. A heating plate was calibrated with K-type self-adhesive thermocouples from Omega (estimated error ±5 °C; time to reach stable temperature ~ 30 s). Spin-coated films were allowed to dry for at least 15 hours at room temperature to remove part of the residual solvent before annealing.

Transmission electron microscopy (TEM)

Samples were prepared by floating off spin-coated films on PEDOT:PSS coated glass substrates in water, followed by collection with TEM copper mesh grids. TEM bright field images, selected area electron diffraction (SAED) patterns and tomography series were recorded with a G2 Tecnai microscope operated at an acceleration voltage of 200 kV. For the TEM bright field images, an under focus of 8 micrometer was used to enhance the contrast in the images. An aperture with the size of 0.8 micrometer was used to collect the SAED pattern. For the tomography series the sample was tilted during collection between -70 and +70 degree tilt with one-degree steps. The reconstructions of the tomography series were done utilizing a "Simultaneous Iterative Reconstruction Technique" (SIRT) algorithm implemented using the software Inspect3D. The EELS spectra were collected with a Gatan Gif system, mounted on a Titan operated at 300 kV in STEM mode.

Results and Discussion

In a first set of experiments, the nanostructure of a spincoated TQ1:PCBM film was studied before and after thermal annealing for 10 min at 120 °C in air, see Fig. 1. Before annealing there are no distinct features in the film and even at higher magnifications the film appears homogeneous, as evident in the inset in Fig 1 (a). Distinct phases may still be present on a small scale that it is not accessible using TEM bright field imaging. Based on our observations the limit for detection is of the order of 30 nm. While the film is thin, around 100 nm, distinct phases are not visible if the domains are small enough and randomly stacked along the axis normal to the surface of the film.

The change in nanostructure upon thermal annealing agrees well with our previous TEM studies of TQ1:fullerene blends.[13, 19] Since the BHJ blend is not thermally stable, upon thermal annealing above T_g TQ1 and PCBM start to phase separate into different domains, giving rise to a coarser structure, as can be seen in the inset in Figure 1 (b). Compared to pristine films prior to annealing, various darker and brighter domains in the size range of 30-40 nm, can now be seen. PCBM and TQ1 are unlikely to separate into pure domains, the darker areas seen in Fig 1 (b) correspond to denser PCBM rich domains and the brighter areas corresponds TQ1 rich domains.[35]

After annealing, several PCBM crystals, with a size ranging from a hundred to several hundreds of nanometers, can be seen in the film, see Fig 1 (b). Around the larger crystals there are distinct halos. These halos stem from the diffusion of PCBM towards the growing crystals. The diffusion of PCBM leads to a region that is thinner than the surrounding film and richer in TQ1, which gives rise to the bright halo that can be seen around the crystals.[40]

Fig 2 shows a TEM bright field image of a crystal and its accompanying SAED pattern. The obtained diffraction pattern indicates that the crystals are indeed crystalline and are in agreement with previous studies of polymer:PCBM blends, supporting the assumption that the features seen in Fig 1 (a) are PCBM crystals.[9, 13, 25, 26] Diffraction patterns were collected for several crystals and all recorded diffraction patterns matched the one that can be seen in Fig 2, albeit rotated by various angles, indicating that the crystals have a preferred orientation relative to the normal of the film surface.

To further verify that the crystals seen in Fig 1 (b) are PCBM crystals, Electron energy loss spectroscopy (EELS) was carried out. Because TQ1 contains sulphur and PCBM does not, the sulphur edge at 160 eV loss was chosen for separation of regions containing TQ1 and PCBM.[13] EELS spectra were collected from (1) two different

crystals, the first crystal 500 nm long along its longest axis and the second 180 nm, (2) the depletion zone surrounding the 500 nm crystal and (3) from a region of the film around twenty micrometres away from the crystals. The EELS spectra from the different regions can be seen in Fig 3. To make it possible to compare the spectra each spectrum has been normalized against the carbon peak. For the film, the depletion zone as well as the 180 nm crystal there is a broad sulfur peak stretching from 160 eV loss to the Carbon edge at 290 eV loss, while in the spectrum from the 500 nm crystal no sulfur peak is visible. The difference between the crystals likely arises because the 180 nm crystal does not fully extend through the film and that there is polymer below or above the crystal. This kind of uncertainty is one of the main drawbacks of two-dimensional projections, which however can be alleviated by using TE tomography. Also as expected, due to the diffusion of PCBM from the depletion zone, the sulfur signal from the depletion zone is stronger then the sulfur signal from the rest of the film.

To investigate where the PCBM crystals are growing in the spin-coated films, TE tomography series were recorded for twenty-one PCBM crystals. Eleven of the crystals were from the film that had been annealed for 10 min at 120 °C and ten of the crystals were from a film that had been annealed for 5 min at 120 °C , this to make it possible to study smaller crystals. The crystals were randomly distributed laterally across the films, with sizes ranging from around 70 nm to around 400 nm. Fig 4 shows one of the crystals and part of the reconstructed volume of said crystal. The reconstruction displays a thin slice along the x-z axis that cuts through the crystal. The rendered volume shows both the crystal, and the surrounding amorphous film. As can be seen, the crystal does not penetrate fully through the whole film down to the substrate. This observation could be confirmed for all crystals in the measurement series, no crystal that only partly penetrates through the films connects with the substrate, but all connect with the surface of the film. Utilizing the reconstructed volume of the crystals, the length of the crystals along their longest horizontal axis was plotted against how far the crystals penetrate through the films and how far the crystals protrude out from the films surface, see Fig 5. Both the penetration and the protrusion were measured from the films surface. A clear trend can be seen in Fig 5, the larger the crystal the further it both penetrates the films and protrudes out from the films surface. The increase in penetration and protrusion follow each other relatively well, at least until the crystal have penetrated all the way down to the films' substrate. It is impossible from the tomography measurements to draw any certain conclusions about the exact location of nucleation sites, but the trend in Fig 5 seems to indicate that the crystals nucleate at the films surface or in the vicinity of the upper surface. This also explains the sulfur signal seen in the EELS spectrum for the 180 nm crystal, see Fig 3.

To gain further insight into the dynamics of PCBM crystal nucleation the nanostructure of the surrounding amorphous film was studied. Since no structure could be resolved in the pristine, spincoated film tomography was only used to study the nanostructure of the annealed, 10 min at 120 °C, film. The reconstructed volume of the denser, fullerene rich regions can be seen in Fig 6. The reconstruction shows that larger aggregates, approximately 15-20 nm in size, can be found growing in the upper part of the film. Further differences between the nanostructure of the upper part of the film and the lower part can be found. Studying individual slices of the reconstruction is the easiest way to see these differences and three slices of the reconstruction can be seen in Fig 7 a-c. Fig 7 a shows a slice of the reconstruction 20 nm down from the film-air interface, while Fig 7 b is a slice 50 nm down and Fig 7 c is 80 nm down. The slices show that there is a larger amount of distinct PCBM rich regions in the upper part of the film and that the amount steadily decreases as one moves down through the film towards the film-substrate interface. The tendency for the aggregates to start forming at the film-air interface mirrors our observations for the PCBM crystals and while it is not possible to compare the vertical composition before annealing with the composition after, it is reasonable to assume that the nucleation and growth of the PCBM crystals and the evolution of the films nanostructure upon annealing is connected.

Previous studies of various polyfluorene:PCBM, P3HT:PCBM and TQ1:PCBM blends, using techniques such as Near-edge X-ray absorption fine structure spectroscopy (NEXAFS), dynamic secondary ion mass spectrometry (SIMS) and ellipsometry have shown that the vertical composition of BHJ blends can be affected by various parameters such as, surface energy, substrate interaction and solvent.[41-47] Specifically, using ellipsometry it has been shown that the amount of PCBM in a TQ1:PCBM blend will strongly affect the vertical composition of a spincoated film. It is intriguing to compare the results obtained in this study with the results obtained by J. Loos et al., who used TE tomography to study the distribution of P3HT in films spincoated from P3HT:PCBM blends.[28, 30] P3HT is a semi-crystalline polymer that forms a network of nanowires when heated, and due to its good photovoltaic performance it has been a popular choice for electron donor in BHJ blends. Using TE tomography, J. Loss et al. found that upon annealing a network of P3HT "nanofibers" can start to form in either the lower part or the upper part of P3HT:PCBM films. Their explanation is that where in the film the nucleation of P3HT starts will depend on the vertical composition, which is influenced by various factors, such as for example the amount of P3HT and the solvent used to spincoat the films. These findings illustrate how TE tomography can be used to study the effect that small differences between particular BHJ blends have upon nucleation and growth of any crystallisable component in the blends.

Conclusions

In this paper we have established that TE tomography can serve as a useful tool for studying the nucleation and growth of PCBM crystals in PCBM:polymer BHJ blends. TE tomography revealed that in the here investigated TQ1:PCBM BHJ blend, PCBM crystals do not nucleate randomly in the bulk of blend. Reconstructions of the three-dimensional structure of the crystals show that as the crystals grow in lateral size the penetration down through and the protrusion out of the film increases and that the crystals have a tendency to nucleate in the upper part of the film, close to the air-surface interface. Tomography was also used to show that, upon thermally annealing, PCBM rich domains start to develop in the upper part of the film, mirroring the nucleation of PCBM crystals in the upper part of the film.

Acknowledgements

"Financial support from the Chalmers Areas of Advance in Materials Science and also Nanoscience and Nanotechnology is gratefully acknowledged as well as funding for advanced electron microscopes from the Knut and Alice Wallenberg Foundation. We are grateful for the contributions concerning evaluation of tomography data with Sara Bals within the framework of the European Union Seventh Framework Programme under Grant Agreement 312483 - ESTEEM2 (Integrated Infrastructure Initiative–I3)."

Notes

[a] Department of Applied Physics, Chalmers University of Technology, 41296 Göteborg, Sweden
[b] Department of Chemical and Biological Engineering, Chalmers University of Technology, 41296 Göteborg, Sweden

References

1. G. Dennler, M. C. Scharber and C. J. Brabec, *Advanced materials*, 2009, 21, 1323-1338.
2. Z. He, C. Zhong, S. Su, M. Xu, H. Wu and Y. Cao, *Nature Photonics*, 2012, 6, 593-597.
3. T. L. Nguyen, H. Choi, S. J. Ko, M. A. Uddin, B. Walker, S. Yum, J. E. Jeong, M. H. Yun, T. J. Shin, S. Hwang, J. Y. Kim and H. Y. Woo, *Energy and Environmental Science*, 2014, 7, 3040-3051.
4. J. Subbiah, B. Purushothaman, M. Chen, T. Qin, M. Gao, D. Vak, F. H. Scholes, X. Chen, S. E. Watkins, G. J. Wilson, A. B. Holmes, W. W. H. Wong and D. J. Jones, *Advanced materials*, 2015, 27, 702-705.
5. J. D. Chen, C. Cui, Y. Q. Li, L. Zhou, Q. D. Ou, C. Li, Y. Li and J. X. Tang, *Advanced materials*, 2015, 27, 1035-1041.
6. L. Ye, S. Zhang, W. Zhao, H. Yao and J. Hou, *Chem Mater*, 2014, 26, 3603-3605.
7. S. H. Liao, H. J. Jhuo, Y. S. Cheng and S. A. Chen, *Advanced materials*, 2013, 25, 4766-4771.
8. Y. H. Liu, J. B. Zhao, Z. K. Li, C. Mu, W. Ma, H. W. Hu, K. Jiang, H. R. Lin, H. Ade and H. Yan, *Nat Commun*, 2014, 5.
9. S. Bertho, I. Haeldermans, A. Swinnen, W. Moons, T. Martens, L. Lutsen, D. Vanderzande, J. Manca, A. Senes and A. Bonfiglio, *Solar Energy Materials and Solar Cells*, 2007, 91, 385-389.
10. S. Bertho, G. Janssen, T. J. Cleij, B. Conings, W. Moons, A. Gadisa, J. D'Haen, E. Goovaerts, L. Lutsen, J. Manca and D. Vanderzande, *Solar Energy Materials and Solar Cells*, 2008, 92, 753-760.
11. C. Muller, J. Bergqvist, K. Vandewal, K. Tvingstedt, A. S. Anselmo, R. Magnusson, M. I. Alonso, E. Moons, H. Arwin, M. Campoy-Quiles and O. Inganas, *Journal of Materials Chemistry*, 2011, 21, 10676-10684.
12. J. Bergqvist, C. Lindqvist, O. Backe, Z. F. Ma, Z. Tang, W. Tress, S. Gustafsson, E. G. Wang, E. Olsson, M. R. Andersson, O. Inganas and C. Muller, *J Mater Chem A*, 2014, 2, 6146-6152.
13. C. Lindqvist, A. Sanz-Velasco, E. G. Wang, O. Backe, S. Gustafsson, E. Olsson, M. R. Andersson and C. Muller, *J Mater Chem A*, 2013, 1, 7174-7180.
14. T. A. Bull, L. S. C. Pingree, S. A. Jenekhe, D. S. Ginger and C. K. Luscombe, *Acs Nano*, 2009, 3, 627-636.
15. J. J. Richards, A. H. Rice, R. D. Nelson, F. S. Kim, S. A. Jenekhe, C. K. Luscombe and D. C. Pozzo, *Advanced Functional Materials*, 2013, 23, 514-522.
16. M. Jorgensen, K. Norrman, S. A. Gevorgyan, T. Tromholt, B. Andreasen and F. C. Krebs, *Advanced materials*, 2012, 24, 580-612.
17. I. Cardinaletti, J. Kesters, S. Bertho, B. Conings, F. Piersimoni, J. D'Haen, L. Lutsen, M. Nesladek, B. Van Mele, G. Van Assche, K. Vandewal, A. Salleo, D. Vanderzande, W. Maes and J. V. Manca, *Journal of Photonics for Energy*, 2014, 4.
18. X. N. Yang, J. K. J. van Duren, R. A. J. Janssen, M. A. J. Michels and J. Loos, *Macromolecules*, 2004, 37, 2151-2158.
19. C. Lindqvist, J. Bergqvist, O. Backe, S. Gustafsson, E. Wang, E. Olsson, O. Inganas, M. R. Andersson and C. Muller, *Applied Physics Letters*, 2014, 104.
20. B. Conings, S. Bertho, K. Vandewal, A. Senes, J. D'Haen, J. Manca and R. A. J. Janssen, *Applied Physics Letters*, 2010, 96.
21. E. Verploegen, R. Mondal, C. J. Bettinger, S. Sok, M. F. Toney and Z. Bao, *Advanced Functional Materials*, 2010, 20, 3519-3529.
22. J. Zhao, A. Swinnen, G. Van Assche, J. Manca, D. Vanderzande and B. Van Mele, *J Phys Chem B*, 2009, 113, 1587-1591.
23. I. Cardinaletti, J. Kesters, S. Bertho, B. Conings, F. Piersimoni, J. D'Haen, L. Lutsen, M. Nesladek, B. Van Mele, G. Van Assche, K. Vandewal, A. Salleo, D. Vanderzande, W. Maes and J. V. Manca, *Journal of Photonics for Energy*, 2014, 4.
24. C. He, D. S. Germack, R. Joseph Kline, D. M. Delongchamp, D. A. Fischer, C. R. Snyder, M. F. Toney, J. G. Kushmerick and L. J. Richter, *Solar Energy Materials and Solar Cells*, 2011, 95, 1375-1381.
25. H. Hoppe, M. Drees, W. Schwinger, F. Schaffler and N. S. Sariciftcia, *Synthetic Metals*, 2005, 152, 117-120.
26. A. Swinnen, I. Haeldermans, M. vande Ven, J. D'Haen, G. Vanhoyland, S. Aresu, M. D'Olieslaeger and J. Manca, *Advanced Functional Materials*, 2006, 16, 760-765.
27. A. Swinnen, I. Haeldermans, P. Vanlaeke, J. D'Haen, J. Poortmans, M. D'Olieslaeger and J. V. Manca, *Eur Phys J-Appl Phys*, 2006, 36, 251-256.
28. S. S. van Bavel, E. Sourty, G. de With and J. Loos, *Nano Lett*, 2009, 9, 507-513.
29. S. S. van Bavel and J. Loos, *Advanced Functional Materials*, 2010, 20, 3217-3234.
30. S. S. van Bavel, M. Barenklau, G. de With, H. Hoppe and J. Loos, *Advanced Functional Materials*, 2010, 20, 1458-1463.
31. J. Loos, E. Sourty, K. B. Lu, G. de With and S. van Bavel, *Macromolecules*, 2009, 42, 2581-2586.
32. J. D. Roehling, K. J. Batenburg, F. B. Swain, A. J. Moule and I. Arslan, *Advanced Functional Materials*, 2013, 23, 2115-2122.
33. S. Barrau, V. Andersson, F. L. Zhang, S. Masich, J. Bijleveld, M. R. Andersson and O. Inganas, *Macromolecules*, 2009, 42, 4646-4650.
34. B. V. Andersson, S. Masich, N. Solin and O. Inganas, *J Microsc-Oxford*, 2012, 247, 277-287.
35. L. T. Hou, E. Wang, J. Bergqvist, B. V. Andersson, Z. Q. Wang, C. Muller, M. Campoy-Quiles, M. R. Andersson, F. L. Zhang and O. Inganas, *Advanced Functional Materials*, 2011, 21, 3169-3175.
36. E. Wang, L. Hou, Z. Wang, S. Hellstrom, F. Zhang, O. Inganas and M. R. Andersson, *Advanced materials*, 2010, 22, 5240-5244.
37. J. E. Carle, M. Jorgensen, M. Manceau, M. Helgesen, O. Hagemann, R. Sondergaard and F. C. Krebs, *Solar Energy Materials and Solar Cells*, 2011, 95, 3222-3226.
38. R. Kroon, R. Gehlhaar, T. T. Steckler, P. Henriksson, C. Müller, J. Bergqvist, A. Hadipour, P. Heremans and M. R. Andersson, *Solar Energy Materials and Solar Cells*, 2012, 105, 280-286.
39. Y. Kim, H. R. Yeom, J. Y. Kim and C. Yang, *Energy & Environmental Science*, 2013, 6, 1909.
40. B. Watts, W. J. Belcher, L. Thomsen, H. Ade and P. C. Dastoor, *Macromolecules*, 2009, 42, 8392-8397.

41. C. M. Bjorstrom, A. Bernasik, J. Rysz, A. Budkowski, S. Nilsson, M. Svensson, M. R. Andersson, K. O. Magnusson and E. Moons, *J Phys-Condens Mat*, 2005, 17, L529-L534.
42. A. S. Anselmo, L. Lindgren, J. Rysz, A. Bernasik, A. Budkowski, M. R. Andersson, K. Svensson, J. van Stam and E. Moons, *Chem Mater*, 2011, 23, 2295-2302.
43. C. M. Bjorstrom, S. Nilsson, A. Bernasik, A. Budkowski, M. Andersson, K. O. Magnusson and E. Moons, *Appl Surf Sci*, 2007, 253, 3906-3912.
44. D. S. Germack, C. K. Chan, B. H. Hamadani, L. J. Richter, D. A. Fischer, D. J. Gundlach and D. M. DeLongchamp, *Applied Physics Letters*, 2009, 94, 233303.
45. Z. Xu, L.-M. Chen, G. Yang, C.-H. Huang, J. Hou, Y. Wu, G. Li, C.-S. Hsu and Y. Yang, *Advanced Functional Materials*, 2009, 19, 1227-1234.
46. M. Campoy-Quiles, T. Ferenczi, T. Agostinelli, P. G. Etchegoin, Y. Kim, T. D. Anthopoulos, P. N. Stavrinou, D. D. C. Bradley and J. Nelson, *Nat Mater*, 2008, 7, 158-164.
47. M. Campoy-Quiles, C. Müller, M. Garriga, E. Wang, O. Inganäs and M. I. Alonso, *Thin Solid Films*, 2014, DOI: 10.1016/j.tsf.2014.02.096.

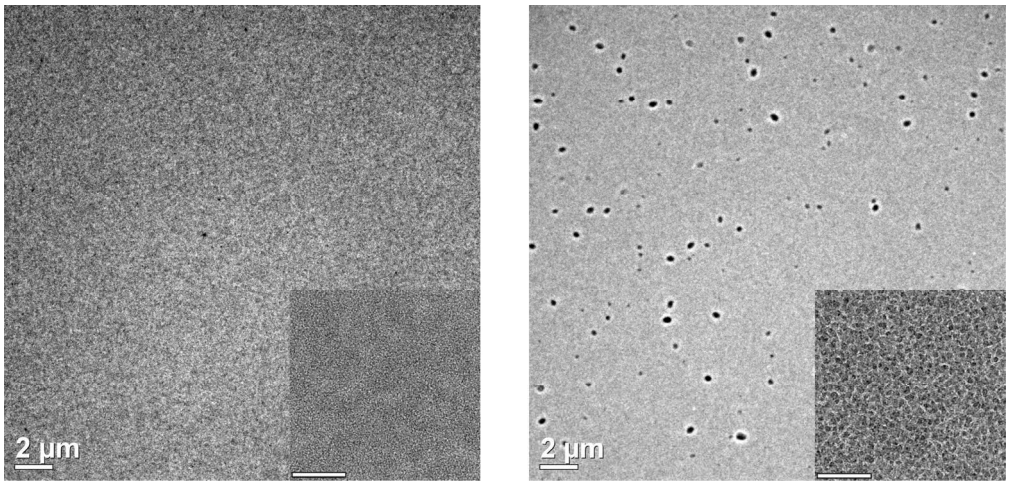

Fig 1. TEM bright field images of (a) a pristine TQ1:PCBM film. (b) film thermally annealed at 120 °C for 10 minutes in air. Inserts: films at higher magnification (the scale bars are 200 nm).
75x35mm (600 x 600 DPI)

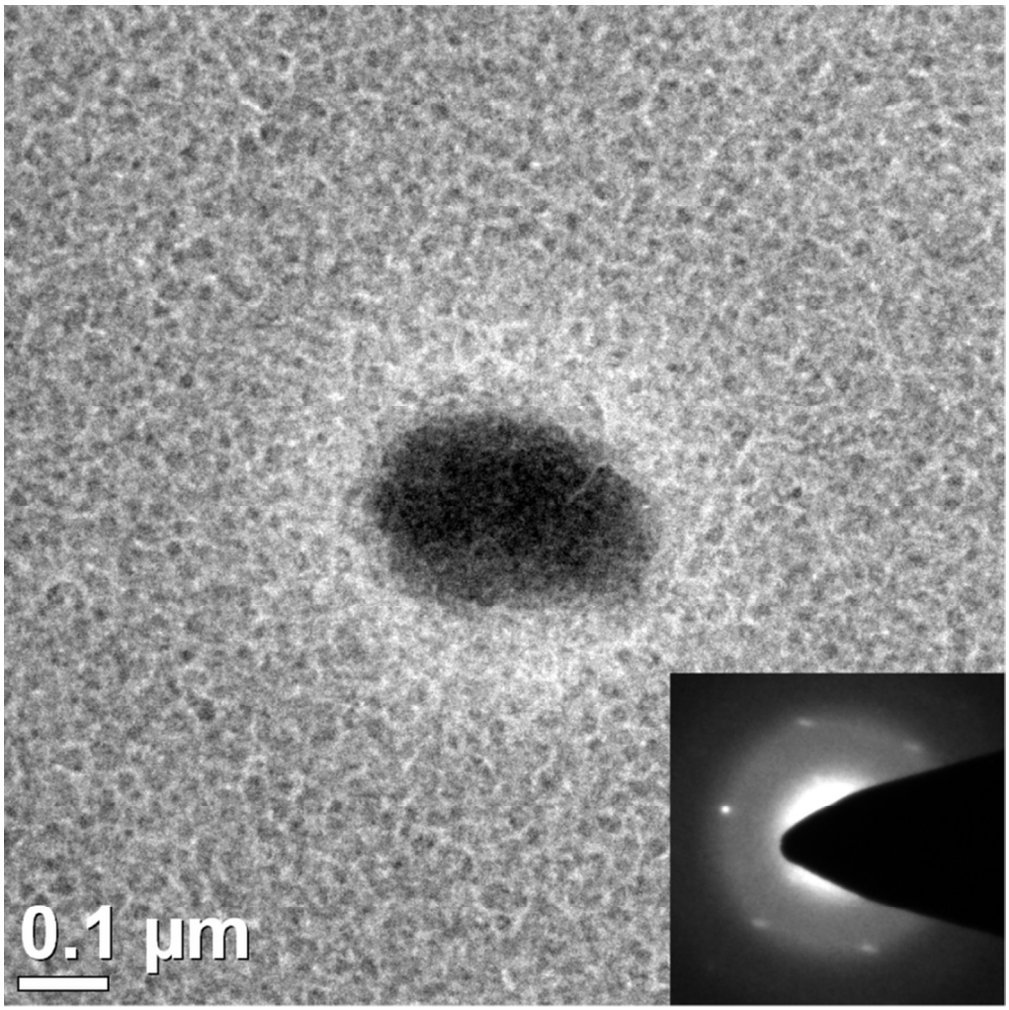

Fig 2. TEM bright field image of a PCBM crystal. Insert: SAED pattern for the crystal and the film surrounding the crystal.
38x38mm (600 x 600 DPI)

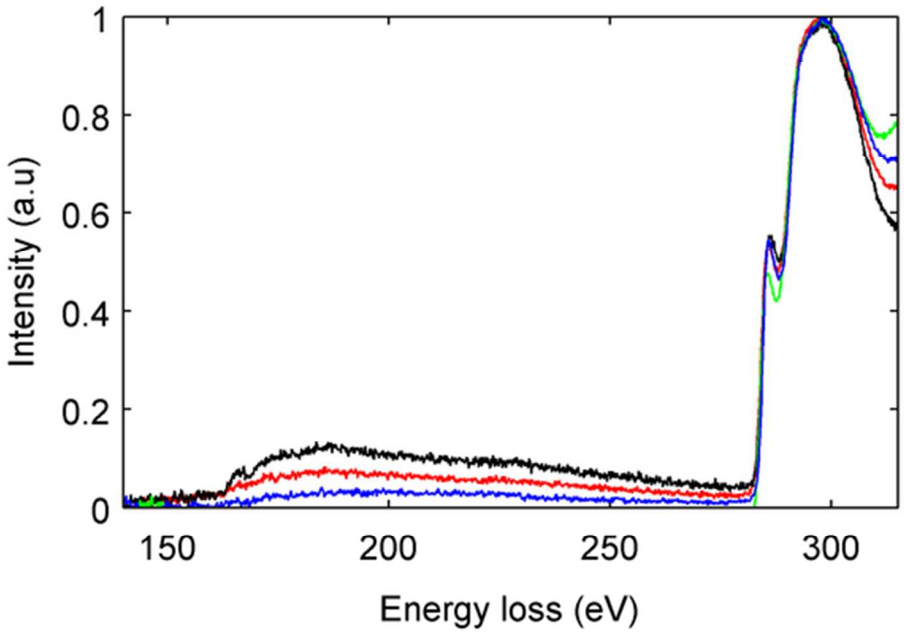

Fig 3. EELS spectra collected from four different regions of an thermally annealed film, (red) the film itself, (black) the depletion zone of a crystal, (green) a 500 nm large PCBM crystal and (**blue**) a 180 nm large PCBM crystal. The intensity has been normalized against the carbon peak.
53x35mm (300 x 300 DPI)

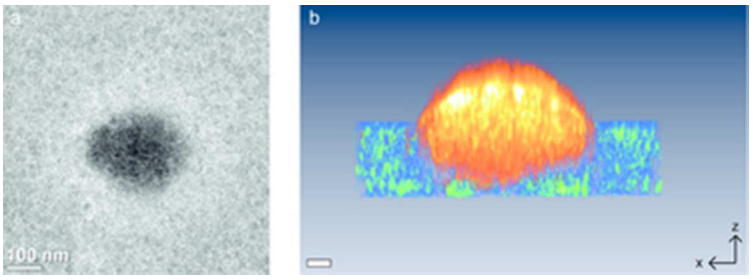

Fig 4. (a) TEM bright field plane view image of a PCBM crystal. (b) A crossection of the tomography reconstruction for said crystal. The rendered volume corresponds to the crystal, orange-yellow, and parts of the film, blue-green. (Scalebar is 30 nm).
31x11mm (300 x 300 DPI)

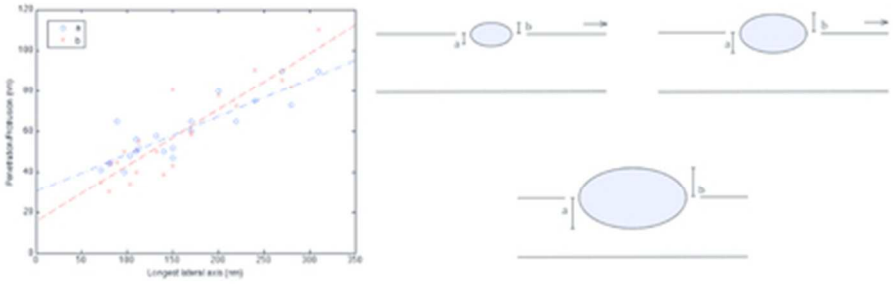

Fig 5. (a) The length of the longest axis of crystals plotted against penetration (a) and protrusion (b) of said crystals, measured from the top surface. (b) Schematic image of how the crystals grow in the film.
19x6mm (600 x 600 DPI)

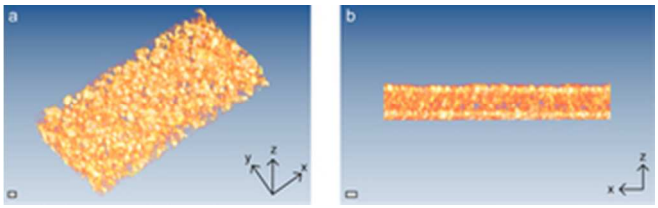

Fig 6. (a) Three dimensional reconstruction the annealed film, the orange-yellow parts corresponds to the denser, PCBM rich domains. (b) A crossection of the reconstruction seen in (a). (The scale bars are 30 nm).
27x8mm (300 x 300 DPI)

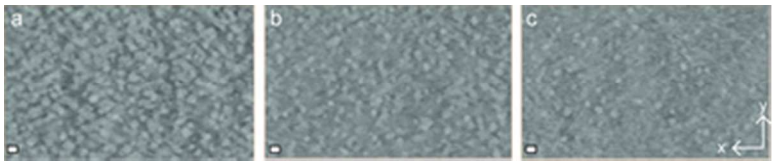

Fig 7. (a) A slice of the tomography reconstruction of the annealed film. The brighter regions correspond to the denser PCBM rich domains, **the contrast is reversed compared to Fig 1**. The slice is **extracted** at 20 nm from the film-air interface. (b) Slice **extracted** 50 nm from the film-air interface. (c) Slice **extracted** 80 nm from the film-air interface. (The scale bars are 30 nm)
16x3mm (600 x 600 DPI)